COMPUTING SPOD FROM FREQUENCY BANDS OF THE FULL-LENGTH DISCRETE FOURIER TRANSFORM

Jakob G. R. von Saldern
Laboratory for Flow Instabilities and Dynamics
Technische Universität Berlin
Berlin, 10623, Germany
j.vonsaldern@tu-berlin.de

Oliver T. Schmidt
Mechanical and Aerospace Engineering
University of California, San Diego
La Jolla, CA 92093, USA

J. Moritz Reumschüssel
Chair of Fluid Dynamics
Technische Universtität Berlin
Berlin, 10623, Germany

Philipp Godbersen
German Aerospace Center (DLR)
Institute of Aerodynamics and Flow Technology
Göttingen, 37073, Germany

Tim Colonius
Department of Mechanical and Civil Engineering
California Institute of Technology
Pasadena, CA 91125, USA

ABSTRACT

This study demonstrates the capabilities of band-ensemble Spectral Proper Orthogonal Decomposition (bSPOD) for investigating the dynamics of broadband–tonal flow cases. Instead of relying on Welch's segmentation formalism, bSPOD estimates modes from frequency bands of a discrete Fourier transform (DFT) of the entire time series, without segmenting the time signal. By making use of the expansion coefficients, which contain information on how much each Fourier mode contributes to a given bSPOD mode, a frequency can be attributed to the mode, yielding improved frequency estimation for broadband–tonal cases. Compared to Welch-based SPOD, the methodology reduces spectral leakage and allows for a variable trade-off between spectral variance and bias across frequencies. In this study, bSPOD is applied to a Mach 0.6 cavity flow subject to aeroacoustic instabilities and to an acoustically forced turbulent jet. The results are compared with those obtained using the classical SPOD algorithm based on Welch segmentation. For both flow cases, bSPOD demonstrates clear advantages in terms of low-bias tonal detection combined with low estimation variance across the entire spectrum.

1 Introduction

Model decomposition techniques are widely used for extracting relevant information from high-dimensional, turbulent flow data (Lumley, 1970; Schmid, 2010; Sieber *et al.*, 2016; Towne *et al.*, 2018). Spectral Proper Orthogonal Decomposition (SPOD) goes back to the work of Lumley (1970) and has recently received considerable attention for its ability to identify coherent structures in turbulent flows that can be related to physical models (Towne *et al.*, 2018). SPOD extracts structures with coherence in time and space and therefore extends the classic space-only POD approach by incorporating temporal information. To compute SPOD modes, one typically relies on Welch's segmentation method to obtain converged statistical estimates (Welch, 1967; Schmidt & Colonius, 2020). This segmentation involves a trade-off: using a small number of long segments achieves high-frequency resolution, but provides only a few mode realizations per frequency bin; using a large number of shorter segments increases the convergence of modes, but can lead to spectral bias and the smearing of sharp tonal peaks.

Several variations and adaptations to SPOD have been developed in recent years. For example, robust SPOD incorporates a robust proper orthogonal decompositon algorithm (Colanera *et al.*, 2025), while shifted SPOD applies time shifting to the snapshot to align advecting structures (Blanco *et al.*, 2022) - both improving statistical convergence. Heidt & Colonius (2024) introduce cyclostationary SPOD to investigate the dynamics evolving around a periodic base state. Yeung & Schmidt (2024) proposed an adaptive SPOD method that does not rely on time segmentation but instead employs a multitaper method. The approach enables control of the bias–variance trade-off across the spectrum through an adaptive algorithm that selects the number of tapers based on a convergence criterion. However, this adaptive formulation requires repeated SPOD computations with varying numbers of tapers, which can become computationally expensive if convergence is to be achieved across the entire spectrum.

To overcome the bias–variance tradeoff, we propose band-ensemble SPOD (bSPOD) in a companion work (von Saldern *et al.*, 2026): modes are computed from narrowly resolved frequency bands of the discrete Fourier transform (DFT) of the full-length time signal, rather than from multitaper or segment-wise Fourier estimates on a coarser frequency grid. The expansion coefficients of the associated eigenvalue problem quantify the contribution of each Fourier bin to each bSPOD mode; these coefficients are used to assign a distinct frequency estimate to each mode. Compared to the commonly used Welch-based method, the approach reduces spectral leakage and enables more accurate frequency estimation of high-energy components at comparable computational cost. It thus provides low-bias estimates of tonal components while maintaining low variance in broadband regions of the spectrum, making it particularly suitable for broadband–tonal flow cases.

In the following, we briefly review the widely used SPOD algorithm based on Welch's time segmentation (Towne *et al.*, 2018; Schmidt & Colonius, 2020) and then introduce the bSPOD method. The effectiveness of bSPOD is subsequently demonstrated using data from a broadband–tonal cavity flow and an acoustically forced jet flow.

2 Spectral POD

We begin with a short overview of the commonly applied SPOD algorithm that uses Welch's segmentation technique (Welch, 1967). We consider a discrete space–time signal $q_{l,n}$ with $l = 0,\dots,N_x-1$ spatial degrees of freedom and $n = 0,\dots,N_t-1$ time samples. In the first step, the time series is divided into N_b blocks of length N_w and transformed into frequency space,

$$\hat{q}^{(b)}_{l,j} = \frac{1}{N_w}\sum_{n=0}^{N_w-1} w_n\, q^{(b)}_{l,n} \exp(-i2\pi jn/N_w)\,, \quad j = 0,\dots,N_w-1 \tag{1}$$

where i is the imaginary unit, b denotes the block number and w_n is a taper (window) used to reduce spectral leakage. A common approach to increase the number of blocks is the use of overlapping time segments; however, this is not considered here for simplicity. The frequency resolution is $\Delta f = 1/(N_w\Delta t)$. For each frequency j, the block-wise Fourier coefficients are stacked into a matrix

$$\mathbf{Q}_j = \left[\hat{\mathbf{q}}^{(1)}_j, \hat{\mathbf{q}}^{(2)}_j, \dots, \hat{\mathbf{q}}^{(N_b)}_j\right], \qquad \hat{\mathbf{q}}^{(b)}_j \in \mathbb{C}^{N_x},\ \ \mathbf{Q}_j \in \mathbb{C}^{N_x\times N_b} \tag{2}$$

From this data matrix $\mathbf{Q}_j$, the cross-spectral density (CSD) matrix is estimated as

$$\mathbf{C}_j = \frac{\alpha}{N_b}\mathbf{Q}_j\mathbf{Q}^*_j, \qquad \alpha = \frac{1}{\Delta f\, U}, \qquad U = \frac{1}{N_w}\sum_{n=0}^{N_w-1} w_n^2 \tag{3}$$

The SPOD modes Φ_j are the eigenvectors of the CSD matrix and the eigenvalues represent power spectral density. This is ensured by the prefactor α in Eq. 3, considering the forward normalization of the Fourier transform, Eq. (1). The eigenvalue problem reads

$$\mathbf{C}_j\mathbf{W}\Phi_j = \Lambda_j\Phi_j, \qquad \Phi^*_j\mathbf{W}\Phi_j = \mathbf{I}, \tag{4}$$

where $\mathbf{W}$ is a weight matrix defining the discretized inner product. When $N_x > N_b$, it is advantageous to solve the alternative eigenvalue problem, known as the method-of-snapshots (Sirovich, 1987)

$$\frac{\alpha}{N_b}\mathbf{Q}^*_j\mathbf{W}\mathbf{Q}_j\Theta_j = \Lambda_j\Theta_j, \qquad \Phi_j = \sqrt{\frac{\alpha}{N_b}}\mathbf{Q}_j\Theta_j\Lambda_j^{-1/2}, \tag{5}$$

i.e., to first solve for the expansion coefficients Θ_j and then to reconstruct the modes by expanding the block-wise Fourier modes using these coefficients. The eigenvalue problem in the method of snapshots is of size $N_b\times N_b$, whereas the corresponding eigenvalue problem based on the CSD matrix is of size $N_x\times N_x$. The modes at frequency index j are assigned the corresponding DFT frequency, $f_j = j\Delta f$. The modes are normalized with respect to the inner product defined in Eq. (4). Their modal power is contained in the SPOD eigenvalues, which represent the power spectral density at the respective frequency. Typically, modes are ranked within each frequency bin, with the most energetic structures being of primary interest.

By combining spectral analysis with proper orthogonal decomposition, SPOD enables the extraction of structures with both spatial and temporal coherence, making it a powerful tool for analyzing coherent structures in broadband turbulent flows across a wide range of fluid mechanics applications (Towne *et al.*, 2018; Lesshafft *et al.*, 2019; Yeung & Schmidt, 2024; von Saldern *et al.*, 2025; Demange *et al.*, 2026). However, the performance of SPOD is often limited by data availability. High frequency resolution requires long block lengths (large N_w), while a large number of blocks (N_b) is required for statistical convergence, particularly for broadband dynamics. Together, these requirements imply that SPOD relies on long time series. In practice, for finite data, one encounters the classical bias–variance trade-off inherent to spectral estimation methods and must balance frequency resolution against statistical convergence. For broadband–tonal flows, this implies that improved convergence in the broadband part of the spectrum comes at the cost of increased bias of tonal components.

3 Band-ensemble SPOD

bSPOD, as introduced in von Saldern *et al.* (2026), addresses the shortcomings of SPOD for broadband–tonal flow cases and enables reduced estimator variance while maintaining low bias of tonal eigenvalue estimates. The method avoids segmentation of the time signal and instead forms ensembles from narrowly resolved frequency bands of the full-length transform. Details of the bSPOD method are provided in the referenced study; here, only the key steps are outlined.

bSPOD is based on the discrete Fourier transform of the full-length signal without time segmentation. Let γ denote the DFT-bin index with physical frequency $f_\gamma = \gamma\widetilde{\Delta f}$, where $\widetilde{\Delta f} = 1/(N_t\Delta t)$ is the fine frequency spacing resulting from the transform of the full record. In analogy to the matrices $\mathbf{Q}_j$ in SPOD, the data matrices $\tilde{\mathbf{Q}}_j$ in bSPOD are formed by collecting N_f adjacent Fourier coefficients anchored at index j, i.e.,

$$\tilde{\mathbf{Q}}_j = \left[\tilde{\mathbf{q}}_{j+1}, \tilde{\mathbf{q}}_{j+2}, \dots, \tilde{\mathbf{q}}_{j+N_f}\right], \qquad \hat{\mathbf{q}}_\gamma \in \mathbb{C}^{N_x},\ \ \tilde{\mathbf{Q}}_j \in \mathbb{C}^{N_x\times N_f}. \tag{6}$$

Similar to the use of overlapping time segments in Welch-based SPOD, the data matrices $\tilde{\mathbf{Q}}_j$ can be constructed from overlapping frequency bands. In the present study, however, we restrict the analysis to the non-overlapping case. From $\tilde{\mathbf{Q}}_j$, the bandwise cross-spectral density is estimated as

$$\tilde{\mathbf{C}}_j = \frac{\tilde{\alpha}}{N_f}\tilde{\mathbf{Q}}_j\tilde{\mathbf{Q}}^*_j, \qquad \tilde{\alpha} = \frac{1}{\widetilde{\Delta f}} \tag{7}$$

A forward normalization of the Fourier transform is assumed in Eq. (7), such that the eigenvalues of the CSD matrix, with the given $\tilde{\alpha}$ factor, represent modal power spectral density. A taper can also be applied, which requires an additional factor of $1/U$, similar to the CSD estimate in Welch-based SPOD (see Eq. (3)). However, in bSPOD, spectral leakage is naturally reduced since the DFT is computed over the entire signal.

As in Welch-based SPOD, the bSPOD modes are the eigenvectors of CSD matrix, $\tilde{\mathbf{C}}_j$. However, the main features of bSPOD rely on the expansion coefficients obtained via the method of snapshots,

$$\frac{\tilde{\alpha}}{N_f}\tilde{\mathbf{Q}}_j^*\mathbf{W}\tilde{\mathbf{Q}}_j\tilde{\Theta}_j = \tilde{\Lambda}_j\tilde{\Theta}_j, \qquad \tilde{\Phi}_j = \sqrt{\frac{\tilde{\alpha}}{N_f}}\tilde{\mathbf{Q}}_j\tilde{\Theta}_j\tilde{\Lambda}_j^{-1/2} \quad (8)$$

where $\mathbf{W}$ defines the inner product, $\tilde{\Lambda}_j$ is the diagonal matrix of bSPOD eigenvalues, and $\tilde{\Phi}_j$ denotes the corresponding modes associated with frequency band j. In Welch-based SPOD, the expansion coefficients Θ_j quantify the contribution of each Fourier mode contained in $\mathbf{Q}_j$ – associated with a time segment – to each SPOD mode (see Eq. (5)). In bSPOD, the expansion coefficients $\tilde{\Theta}_j$ have a similar interpretation, quantifying the contribution of each Fourier mode to each bSPOD mode, Eq. 8. The key difference is that the Fourier modes in $\tilde{\mathbf{Q}}_j$ originate from adjacent frequency bins of the full-length DFT, rather than from different time segments, and are therefore each associated with a unique frequency. The information contained in the expansion coefficients is used to assign each bSPOD mode a frequency estimate. To this end, weights are defined as

$$\beta_{\eta,\gamma} = \frac{\left|\tilde{\theta}_{\gamma,\eta}\right|^{\ell}}{\sum_{\gamma'=1}^{N_f}\left|\tilde{\theta}_{\gamma',\eta}\right|^{\ell}}, \qquad \sum_{\gamma=1}^{N_f}\beta_{\eta,\gamma} = 1 \quad (9)$$

which are then used to compute the modal frequencies as

$$\tilde{\mathbf{f}}_j = \beta\,\mathbf{f}_j, \qquad \mathbf{f}_j = \left[f_{j+1}, f_{j+2}, \ldots, f_{j+N_f}\right]^{\top} \quad (10)$$

where $\mathbf{f}_j$ contains the frequencies of the N_f discrete Fourier modes in the band of index j. The exponent ℓ in Eq. (10) is an adjustable parameter that controls how the contributions of the Fourier modes to a bSPOD mode are mapped to its frequency attribution. A natural choice is $\ell = 1$, corresponding to a contribution-weighted average, in which each frequency is weighted by the contribution of its associated DFT mode. For $\ell = 0$, all frequencies within the band are weighted equally, such that the band-center frequency is recovered. In the limit $\ell \to \infty$, the bSPOD mode is assigned the frequency of the most contributing DFT mode, which is a suitable choice for precise frequency estimation of tonal components.

For broadband–tonal flows, it is advantageous to choose $\ell = 1$ in the broadband part of the spectrum and $\ell = \infty$ in the vicinity of tonal components. This yields a well-resolved frequency grid in broadband regions while ensuring accurate frequency estimation of tonal components. Accordingly, in this study, $\ell = 1$ is used as the default value, and $\ell = \infty$ is selected when a tonal component is detected in the current or adjacent frequency bands. Tonal components are identified based on the relative change in eigenvalue magnitude between adjacent frequencies; a tonal component is detected if this change exceeds a threshold, here set to 50%. When overlapping bands are considered, $\ell = \infty$ is applied in every band that contains the tonal component.

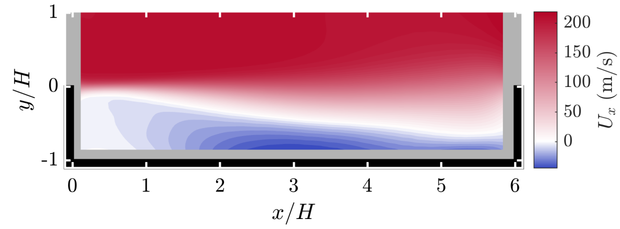

Figure 1. Time-averaged axial velocity component of the cavity flow. The thick black line indicates the cavity wall.

The parameter N_f plays a role analogous to the number of blocks N_b in Welch-based SPOD: increasing N_f (i.e., including more DFT modes per band) enhances averaging and improves statistical convergence (reduces variance). For $N_f = N_b$, both methods estimate the CSD matrix over the same effective bin width $\Delta f = N_f\widetilde{\Delta f}$, and the resulting matrices are of the same size, yielding the same number of SPOD eigenvalues and eigenvectors. Under the assumption that the dynamics do not vary across this bin width and neglecting spectral leakage, both methods are expected to produce equivalent results. The key difference relative to Welch-based SPOD is twofold: reduced spectral leakage due to the use of the full-length DFT and improved frequency attribution. Tonal modes concentrate energy in a few DFT bins, and the expansion coefficients capture this concentration, enabling accurate frequency estimation for each bSPOD mode. Combined with the reduced spectral leakage, bSPOD allows improving statistical convergence without sacrificing frequency localization of tonal components. In addition to these advantages, the bandwidth N_f can be varied with frequency, allowing for an adaptable bias–variance trade-off similar to the multitaper approach of Yeung & Schmidt (2024).

4 Results

To highlight the features of bSPOD, we apply it to two broadband–tonal flow cases and compare the results with Welch-based SPOD, in the following simply referred to as SPOD. The first example is a mono-PIV dataset of a Mach 0.6 cavity flow recorded by Zhang *et al.* (2020), which exhibits aeroacoustic instabilities and was also considered in our previous bSPOD study (von Saldern *et al.*, 2026). The second example is a mono-PIV dataset of an acoustically forced round turbulent jet at a Reynolds number of 10,000, reported by Reumschüssel *et al.* (2024).

4.1 Cavity flow

The cavity flow dataset of Zhang *et al.* (2020) comprises 16,000 velocity snapshots obtained from mono-PIV measurements at an acquisition rate of 16 kHz. The measurement plane is located at the cavity center plane. The rectangular cavity has a height of $H = 26.5$ mm, a length-to-depth ratio of $L/H = 6$, and an out-of-plane depth of $3.85H$. The broadband flow exhibits additional tonal components, known as Rossiter modes, arising from an aeroacoustic instability mechanism. For further details on the experimental setup, the reader is referred to the original publication (Zhang *et al.*, 2020). Figure 1 shows the mean axial velocity U_x, obtained by averaging all 16,000 snapshots.

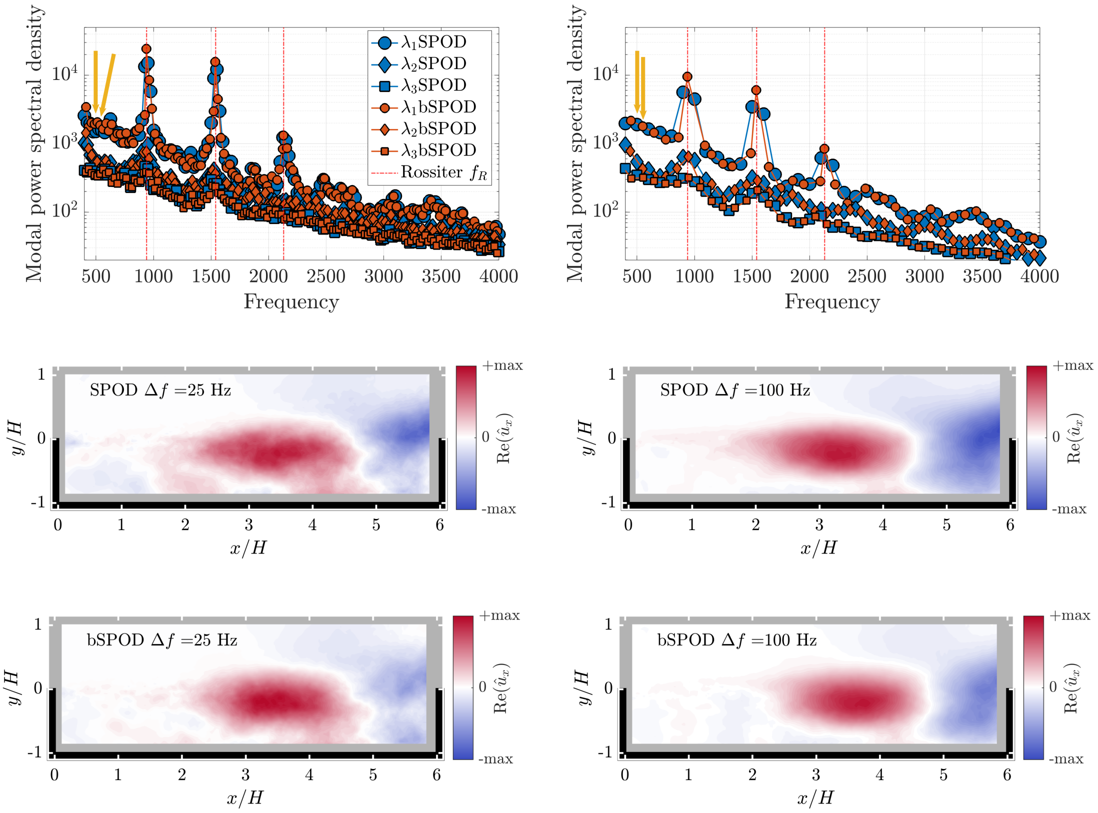

Figure 2. Comparison between Welch-based SPOD and bSPOD for the cavity flow at two frequency resolutions: left $\Delta f = 25$ Hz, right $\Delta f = 100$ Hz. The top panels show the leading three eigenvalues for both methods. The middle and bottom panels display the real part of the axial velocity mode at 500Hz, indicated by the yellow arrow in the top panels, for SPOD and bSPOD, respectively.

For the analysis of coherent structures, SPOD and bSPOD are applied to the fluctuating velocity field obtained by subtracting the temporal mean from the velocity snapshots. The modal decompositions are compared for $N_f = N_b$, such that the number of blocks in Welch-based SPOD corresponds to the number of consecutive modes in bSPOD. This ensures a fair comparison between the methods, as the modes are computed with the same frequency resolution.

The top panel in the left column of Fig. 2 shows the SPOD and bSPOD eigenvalue spectra for $N_f = N_b = 25$, corresponding to a frequency resolution of $\Delta f = 25$ Hz. The three most dominant eigenvalues are shown. The frequencies of the Rossiter tones are indicated by red vertical lines, obtained from the power spectral density of a pointwise velocity probe located in the shear layer at $y/H = 0$ and $x/H = 2$. At this frequency resolution, SPOD and bSPOD yield similar results and capture the instabilities reasonably well. However, the variance of the eigenvalue estimates remains high for both methods, indicating insufficient convergence and the need for increased averaging.

The second and third panels in the left column of Fig. 2 show the real part of the axial velocity mode at 500 Hz. The corresponding eigenvalues at this comparatively low frequency are highlighted in the spectrum by a yellow arrow. The mode shapes obtained from SPOD and bSPOD are of similar quality and both exhibit a relatively high noise level. This observation further indicates limited convergence of the analysis.

To improve convergence, N_f and N_b are increased to 100, yielding an effective frequency resolution of $\Delta f = 100$ Hz. The corresponding eigenvalue spectra and low-frequency modes are shown in the right column of Fig. 2. For both methods, a substantial reduction in the variance of the eigenvalue estimates is observed, and the low-frequency mode shapes exhibit improved convergence. For Welch-based SPOD, the reduction in variance comes at the cost of increased spectral bias of the Rossiter tone frequencies. In contrast, bSPOD provides accurate eigenvalue estimates of the Rossiter modes even at this relatively large bin width of 100 Hz. This improvement is attributed to reduced spectral leakage, which mitigates the smearing of tonal energy across frequency bins, and to the frequency attribution, which enables accurate estimation of the tonal frequency within the 100 Hz bands.

4.2 Turbulent round jet flow

The second flow configuration used to assess the capabilities of bSPOD is a jet flow at Reynolds number 10,000 (2.93 m/s bulk velocity) that emerges from a nozzle of diameter $D = 51$ mm. The nozzle is equipped with eight zero-net mass flux actuators, arranged circumferentially around the outlet. The actuators each consist of an acoustic driver that is connected through a rectangular channel with a slit close to the nozzle lip. By running the drivers, the shear layers of the jet can be forced. The circumferential arrangement allows forcing at different circumferential wavenumbers m through control of the phase difference between the driver's signals. Reumschüssel *et al.* (2024) used Bayesian optimization on this setup to identify forcing patterns that maximize entrainment and analyzed the underlying physics. More details can be found in the referenced article. In this study, we investigate two of their configurations using bSPOD; the unforced jet flow and a forced case, with combined axisymmetric ($m = 0$) and helical $m = 1$ forcing, superposed at two different frequencies. For each of the configurations, we analyze a dataset of

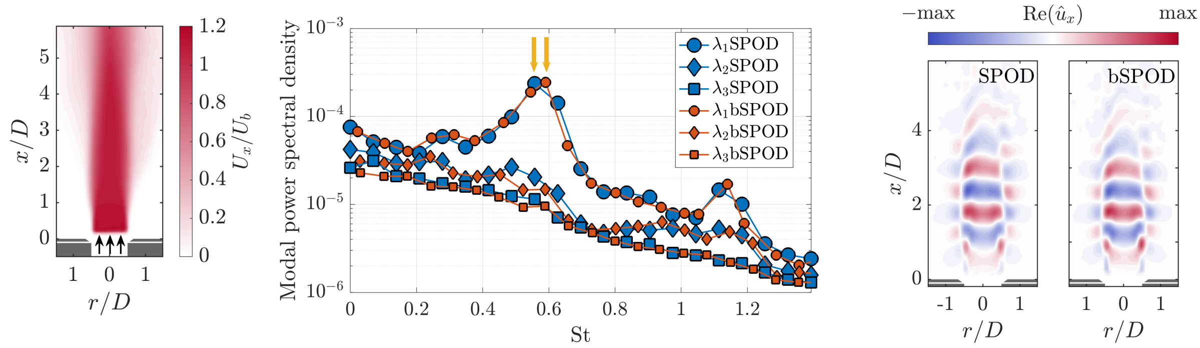

Figure 3. Left: Time-averaged axial velocity component of the unforced jet flow. Grey regions in the upstream area indicate the nozzle, while the white slits denote the channels connected to the loudspeakers. Middle: SPOD and bSPOD eigenvalue spectra (three dominant eigenvalues shown). Right: Real part of the axial velocity mode at St ≈ 0.59 (highlighted with yellow arrows).

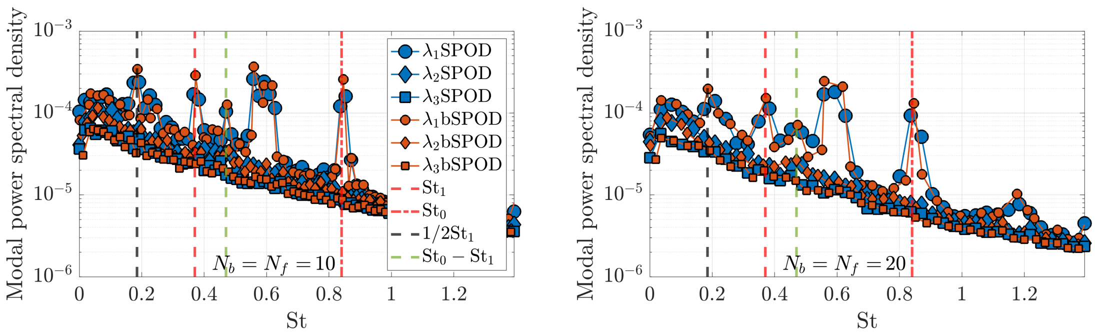

Figure 4. SPOD and bSPOD eigenvalue spectra for the three dominant eigenvalues, computed for $N_b = N_f = 10$ (left) and $N_b = N_f = 20$ (right). Vertical lines indicate the forcing frequencies (red) and nonlinear interaction frequencies (black and green).

10,000 snapshots of the two-dimensional velocity fields, acquired from mono-PIV at a sampling rate of 1 kHz.

The left panel in Fig. 3 shows the time-averaged axial velocity of the jet flow without acoustic forcing. It shows shear layers that emerge at the nozzle tip between the jet flow and the surrounding air. These grow in axial direction and enclose a potential core of around 5-6 nozzle diameters length in which the bulk velocity is roughly maintained. The middle panel in Fig. 3 shows the SPOD and bSPOD eigenvalue spectra for $N_b = N_f = 40$, corresponding to a frequency resolution of $\Delta\mathrm{St} = 0.07$ ($\Delta f = 4$ Hz), where the Strouhal number is defined based on the nozzle diameter and bulk flow velocity. The leading three eigenvalues are shown. For this unforced flow, SPOD and bSPOD yield very similar eigenvalue spectra. In the frequency range $0.4 \leq \mathrm{St} \leq 0.6$, an elevation of the leading eigenvalue is observed. This is consistent with the dynamics of turbulent round jets, which are dominated by Kelvin–Helmholtz-type vortex shedding in this frequency range. The right panel shows the real part of the axial velocity mode corresponding to the dominant eigenvalue for both SPOD and bSPOD, highlighted by a yellow arrow in the spectrum. The mode shape exhibits the characteristic Kelvin–Helmholtz wavepacket structure. At approximately twice this characteristic frequency, $\mathrm{St} \approx 1.1$, another elevation in the leading eigenvalue is observed, likely corresponding to a higher harmonic of the Kelvin–Helmholtz-type modes. The overall similarity in eigenvalue spectra and mode shapes highlights the consistency of both methods for broadband flow features.

Next, we analyze the flow field under acoustically forced conditions. Using the circumferentially arranged speakers, the flow is simultaneously forced with an $m = 1$ azimuthal mode at $\mathrm{St}_1 = 0.37$ and an $m = 0$ mode at $\mathrm{St}_0 = 0.84$. Figure 4 shows the three most dominant eigenvalues computed from the corresponding mono-PIV snapshots using SPOD and bSPOD. The left panel presents the eigenvalue spectra for $N_f = N_b = 10$, corresponding to a frequency resolution of $\Delta\mathrm{St} = 0.017$ ($\Delta f = 1$ Hz), while the right panel shows the results for $N_f = N_b = 20$, i.e., for more modes per frequency bin and thus a reduced frequency resolution of $\Delta\mathrm{St} = 0.035$ ($\Delta f = 2$ Hz).

Compared to the unforced case, the eigenvalue spectrum changes significantly. Distinct peaks appear at the forcing frequencies (highlighted by red vertical lines), while the broadband elevation of the leading eigenvalue is confined to a narrower frequency range between $\mathrm{St} \approx 0.5$ and $\mathrm{St} \approx 0.6$. In addition to the primary forcing peaks, further peaks are observed at $\mathrm{St}_1/2$ (black) and $\mathrm{St}_0 - \mathrm{St}_1$ (green), indicative of nonlinear interactions. A comparison between SPOD and bSPOD shows that these tonal components, and in particular their frequencies, are captured more accurately by bSPOD. In Welch-based SPOD, the tones are more difficult to identify, as spectral leakage and the fixed frequency grid smear the tonal energy across neighboring frequency bins. In contrast, bSPOD reduces leakage and, through improved frequency attribution, enables more accurate resolution of all tonal modes. This improvement is already evident at the higher frequency resolution shown in the left panel and becomes even more pronounced for the more converged spectrum with lower frequency resolution shown in the right panel.

Figure 5 shows the real part of the axial velocity mode shape corresponding to the leading bSPOD eigenvalue for the four highlighted frequencies in the right panel of Fig. 4 ($N_f =$

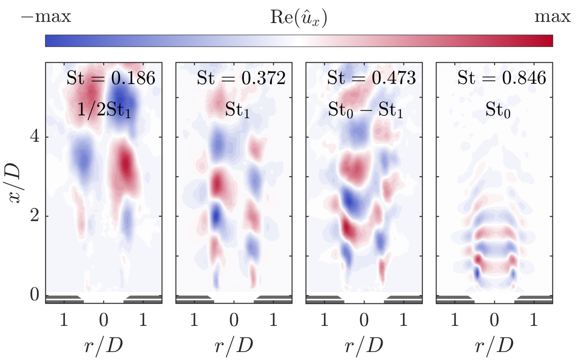

Figure 5. Real part of axial velocity mode for bSPOD with $N_f = 20$, highlighted with vertical lines in right panel of Fig. 4. Each mode is normalized by its respective maximum value.

20). For St_0, the axial velocity mode shape is symmetric with respect to the centerline. For St_1, it is anti-symmetric. This is expected for axisymmetric ($m = 0$) and azimuthal ($m = 1$) forcing, respectively. The two additional mode shapes at $\mathrm{St}_1/2$ and $\mathrm{St}_0 - \mathrm{St}_1$ are also predominantly anti-symmetric, although the symmetry of the latter is less pronounced.

The frequencies identified via bSPOD frequency attribution are indicated at the top of each panel in Fig. 5 (rounded). The results show that the mode identified as $\mathrm{St}_1/2$ is accurately located at half the forcing frequency St_1, and that the mode labeled $\mathrm{St}_0 - \mathrm{St}_1$ precisely matches the difference between the forcing frequencies. This provides strong evidence that these modes arise from non-linear mode coupling, in which the frequencies and azimuthal wavenumbers result from an additive combination. The accurate reproduction of this characteristic highlights the precise frequency identification provided by bSPOD. Such information is not readily accessible from SPOD based on Welch's segmentation, highlighting the advantages of bSPOD for the analysis of nonlinear interactions in broadband–tonal flow cases.

5 Conclusion

In this study, we compared the novel method of band-ensemble SPOD (bSPOD), which computes modes from frequency bands of the full-length Fourier transform to SPOD based on Welch's time-segmentation approach. bSPOD offers reduced spectral leakage and improved frequency estimation of the modes by exploiting the expansion coefficients, which quantify the contribution of each Fourier mode to a given bSPOD mode. These advantages are particularly beneficial for broadband–tonal flow cases, where estimation variance can be reduced while maintaining low bias in the identification of tonal components.

The capabilities of bSPOD were demonstrated for a Mach 0.6 cavity flow exhibiting aeroacoustic instabilities and for a turbulent round jet subject to simultaneous acoustic forcing at two frequencies with different azimuthal mode structures. The results show that bSPOD provides a more accurate representation of tonal components and their interactions. In particular, for the forced jet case involving nonlinear mode coupling, bSPOD enables clear identification of the tones and their triadic interactions, whereas in Welch-based SPOD the energy is smeared across neighboring frequency bins and the fixed frequency grid limits accurate tracking of such interactions.

REFERENCES

Blanco, Diego C.P., Martini, Eduardo, Sasaki, Kenzo & Cavalieri, André V.G. 2022 Improved convergence of the spectral proper orthogonal decomposition through time shifting. *Journal of Fluid Mechanics* **950**, A9.

Colanera, Antonio, Schmidt, Oliver T. & Chiatto, Matteo 2025 Robust spectral proper orthogonal decomposition. *Computer Physics Communications* **307**, 109432.

Demange, Simon, Oberleithner, Kilian, Yuan, Zhenyang, Hanifi, Ardeshir & Cavalieri, André V. G. 2026 Flow structures driving broadband trailing-edge noise: A resolvent-based model. *AIAA Journal* **64** (3), 1414–1426.

Heidt, Liam & Colonius, Tim 2024 Spectral proper orthogonal decomposition of harmonically forced turbulent flows. *Journal of Fluid Mechanics* **985**, A42.

Lesshafft, Lutz, Semeraro, Onofrio, Jaunet, Vincent, Cavalieri, André V. G. & Jordan, Peter 2019 Resolvent-based modeling of coherent wave packets in a turbulent jet. *Physical Review Fluids* **4** (6), 063901.

Lumley, John L. 1970 *Stochastic tools in turbulence*. Academic Press.

Reumschüssel, J. Moritz, Li, Yiqing, zur Nedden, Philipp M., Wang, Tianyu, Noack, Bernd R. & Paschereit, C. Oliver 2024 Experimental jet control with bayesian optimization and persistent data topology. *Physics of Fluids* **36** (9), 095164.

von Saldern, Jakob G. R., Beuth, Jan P., Reumschüssel, Johann Moritz, Jaeschke, Alexander, Paschereit, Christian Oliver & Oberleithner, Kilian 2025 Low-frequency streaky structures in turbulent hydrogen jet flames. *Combustion and Flame* **278**, 114231.

von Saldern, Jakob G. R., Schmidt, Oliver T., Godbersen, Philipp, Reumschüssel, J. Moritz & Colonius, Tim 2026 Band-ensemble spectral proper orthogonal decomposition with frequency attribution. *arXiv preprint arXiv:2602.06588* .

Schmid, Peter J. 2010 Dynamic mode decomposition of numerical and experimental data. *Journal of Fluid Mechanics* **656**, 5–28.

Schmidt, Oliver T. & Colonius, Tim 2020 Guide to spectral proper orthogonal decomposition. *AIAA Journal* **58** (3), 1023–1033.

Sieber, Moritz, Paschereit, C. Oliver & Oberleithner, Kilian 2016 Spectral proper orthogonal decomposition. *Journal of Fluid Mechanics* **792**, 798–828.

Sirovich, Lawrence 1987 Turbulence and the dynamics of coherent structures. I. Coherent structures. *Quarterly of applied mathematics* **45** (3), 561–571.

Towne, Aaron, Schmidt, Oliver T. & Colonius, Tim 2018 Spectral proper orthogonal decomposition and its relationship to dynamic mode decomposition and resolvent analysis. *Journal of Fluid Mechanics* **847**, 821–867.

Welch, Peter 1967 The use of fast fourier transform for the estimation of power spectra: a method based on time averaging over short, modified periodograms. *IEEE Transactions on Audio and Electroacoustics* **15** (2), 70–73.

Yeung, Brandon C. Y. & Schmidt, Oliver T. 2024 Adaptive spectral proper orthogonal decomposition of broadband-tonal flows. *Theoretical and Computational Fluid Dynamics* **38**, 355–374.

Zhang, Yang, Cattafesta, Louis N. & Ukeiley, Lawrence 2020 Spectral analysis modal methods (samms) using non-time-resolved piv. *Experiments in Fluids* **61** (11), 226.